

See discussions, stats, and author profiles for this publication at: <https://www.researchgate.net/publication/355284107>

# In Situ Study of Reduction of $\text{Mn}_x\text{Co}_{3-x}\text{O}_4$ Mixed Oxides: The Role of Manganese Content

Article in *Inorganic Chemistry* · October 2021

DOI: 10.1021/acs.inorgchem.1c02379

CITATIONS

10

READS

158

8 authors, including:



**Olga Alexandrovna Bulavchenko**

Boreskov Institute of Catalysis

157 PUBLICATIONS 2,862 CITATIONS

[SEE PROFILE](#)



**Vasily Kaichev**

Boreskov Institute of Catalysis

254 PUBLICATIONS 6,615 CITATIONS

[SEE PROFILE](#)

This document is confidential and is proprietary to the American Chemical Society and its authors. Do not copy or disclose without written permission. If you have received this item in error, notify the sender and delete all copies.

### **In situ Study of Reduction of $\text{Mn}_x\text{Co}_{3-x}\text{O}_4$ Mixed Oxides: the Role of Manganese Content**

Journal:	<i>Inorganic Chemistry</i>
Manuscript ID	ic-2021-02379u.R2
Manuscript Type:	Article
Date Submitted by the Author:	28-Sep-2021
Complete List of Authors:	<p>Bulavchenko, Olga; Institut kataliza imeni GK Boreskova SO RAN, Afonassenko, Tatyana; Center of New Chemical Technologies of the Boreskov Institute of Catalysis of SB RAS</p> <p>Ivanchikova, Anastasya; Boreskov Institute of Catalysis SB RAS; Novosibirsk State University</p> <p>Murzin, Vadim; Deutsches Elektronen-Synchrotron, FS-PEX</p> <p>Kremneva, Anna; Boreskov Institute of Catalysis SB RAS</p> <p>Saraev, Andrey; Boreskov Institute of Catalysis SB RAS,</p> <p>Kaichev, Vasily; Boreskov Institute of Catalysis SB RAS</p> <p>Tsybulya, Sergey; Boreskov Institute of Catalysis SB RAS; Novosibirsk State University</p>

SCHOLARONE™  
Manuscripts

# *In situ* Study of Reduction of $\text{Mn}_x\text{Co}_{3-x}\text{O}_4$ Mixed Oxides: the Role of Manganese Content

*Olga A. Bulavchenko,<sup>†,‡,\*</sup> Tatyana N. Afonassenko<sup>⊥</sup>, Anastasya V. Ivanchikova,<sup>†,‡</sup>*

*Vadim Yu. Murzin<sup>§</sup>, Anna M. Kremneva,<sup>†</sup> Andrey A. Saraev<sup>†</sup>, Vasily V. Kaichev<sup>†</sup>, and*

*Sergey V. Tsybulya<sup>†,‡</sup>*

<sup>†</sup>Boriskov Institute of Catalysis, Ak. Lavrentiev Avenue, 5, Novosibirsk 630090, Russia

<sup>‡</sup>Novosibirsk State University, Pirogov Street, 2, Novosibirsk 630090, Russia

<sup>⊥</sup>Center of New Chemical Technologies BIC, Omsk 644040, Russia

<sup>§</sup>Deutsches Elektronen-Synchrotron, DESY, Hamburg D-22607, Germany

\* [obulavchenko@catalysis.ru](mailto:obulavchenko@catalysis.ru)

**ABSTRACT:** A series of Mn-Co mixed oxides with a gradual varying of the Mn/Co molar ratio was prepared by coprecipitation of cobalt and manganese nitrates. The structure, chemistry, and

reducibility of the oxides were studied by X-ray diffraction (XRD), X-ray absorption spectroscopy (XAS), X-ray photoelectron spectroscopy (XPS), and temperature programmed reduction (TPR).

It was found that at concentrations of Mn below 37 at.%, a solid solution has a structure of a cubic spinel. At concentrations above 63 at.%, a solid solution is formed on the basis of the tetragonal spinel, while at the concentrations in a range 37–63 at.%, a two-phase system, which contains tetragonal and cubic oxides, is formed. To elucidate the reduction route of mixed oxides, two approaches were used. First of them was based on a gradual change in the chemical composition of Mn-Co oxide illustrating the slow changes in the TPR profiles. The second approach consisted in the combination of *in situ* XRD and *pseudo in situ* XPS techniques, which made it possible to directly determine the structure and chemistry of the oxides under reductive conditions. It was shown that the reduction of Mn-Co mixed oxides proceeds via two stages. During the first stage,  $(\text{Mn,Co})_3\text{O}_4$  is reduced to  $(\text{Mn,Co})\text{O}$ . During the second stage, solid solution  $(\text{Mn,Co})\text{O}$  is transformed to metallic cobalt and MnO. The introduction of manganese cations into the structure of cobalt oxide leads to a decrease in the rate of both reduction stages. However, the influence of additional cations on the second reduction stage is more noticeable. This is due to crystallographic peculiarities of the compounds: the conversion from the initial oxide  $(\text{Mn,Co})_3\text{O}_4$  into the

intermediate oxide (Mn,Co)O requires only a small displacement of cations, whereas the formation of metallic cobalt from (Mn,Co)O requires a rearrangement of the entire structure.

## 1. INTRODUCTION

The reduction of metal oxides is one of the most important issues of solid-state chemistry, which includes investigations of chemical and phase transformations during oxygen removal (for example, under H<sub>2</sub>, CO, or CH<sub>4</sub> flows or interacting with liquid and solid reagents). A detailed knowledge of the reducibility of oxides is important not only from a fundamental point of view; it is also widely used in industries such as metallurgy, catalysis, and electronics. The reducibility of oxides is an essential characteristic of catalysts used in many different reactions. First, it is important for oxidation reactions following the Mars-van Krevelen mechanism<sup>1-4</sup>, in which mobile lattice oxygen of transition metal oxides takes part in the oxidation of reactants. In this case, the reducibility of the oxide catalyst determines the tendency of the oxide to lose oxygen or to donate it to substrates. Second, the oxide reduction can be an activation stage of the Fischer-Tropsch synthesis<sup>5-8</sup>, water-gas shift reaction<sup>9-11</sup>, and oxidative dehydrogenation of hydrocarbons<sup>12, 13</sup>. In this case, the activation of catalysts leads to the transformation of active species from an oxidized state to the metallic state, and depending on the reductive conditions, the active states can be

changed drastically. Third, under reductive conditions, it is possible to create unique types of active states of catalysts due to nanoparticle exsolution onto the surface of mixed oxides <sup>14, 15</sup>.

The reduction of simple oxides, such as  $\text{Fe}_2\text{O}_3$ ,  $\text{NiO}$ ,  $\text{CuO}$ ,  $\text{Co}_3\text{O}_4$ , and  $\text{Mn}_3\text{O}_4$ , has been widely studied <sup>16-22</sup>. In contrast, in the case of mixed oxides, there is lack of understanding. In general, the presence of two metals in the oxide structure can lead to the formation of new intermediate oxides during the reduction. Moreover, the introduction of an additional element can lead to slowdown or acceleration of chemical reactions and to the appearance of cations in unusual coordinations. In this work, we studied the effect of doping of cobalt oxide with manganese cations on its reducibility. Co-Mn mixed oxides demonstrate a high catalytic activity in the oxidation of CO <sup>23-25</sup> and volatile organic compounds <sup>26, 27</sup>; they are employed also in bifunctional electrocatalysts <sup>28</sup> and as precursors of catalysts for the Fischer-Tropsch synthesis <sup>29-31</sup>. Understanding the pathways of reduction and the influence of additives will help to improve the catalytic performance and elucidate the nature of the active sites. The knowledge of the reduction of mixed Mn-Co oxides is rather scarce, and most of it is focused on studies of supported catalysts <sup>8, 27, 32, 33</sup>. Previously, we have investigated structural transformations occurring during the reduction of a two-phase system consisting of  $\text{MnCo}_2\text{O}_4$  and  $\text{CoMn}_2\text{O}_4$  with a total molar ratio Mn : Co = 1 : 1 in comparison with

the simple oxides  $\text{Co}_3\text{O}_4$  and  $\text{Mn}_3\text{O}_4$  <sup>34</sup>. Herein, the reduction of a series of  $\text{Mn}_x\text{Co}_{3-x}\text{O}_4$  solid solutions with a gradual variation in the chemical composition was studied *in situ* by XRD, XPS, and TPR.

## 2. EXPERIMENTAL SECTION

Samples with the different Co:Mn molar ratio were prepared by the coprecipitation method. A calculated amount of  $\text{Co}(\text{NO}_3)_2$  and  $\text{Mn}(\text{NO}_3)_2$  aqueous solutions was poured into a round-bottom flask. Precipitation was carried out under stirring with a gradual addition of a NaOH solution to bring pH of the solution to 11. After subsequent aging, the precipitate was filtered, washed with distilled water on a filter to pH = 6, and dried at 120 °C. Then the sample was calcined in air at 600 °C for 4 h. The resulting samples were referred to as  $\text{Mn}_x\text{Co}_{3-x}$  ( $x=0.1-2.9$ ), where  $x/(3-x)$  is the ratio between Mn and Co cations.

The phase composition of fresh samples was studied by XRD using a Thermo X'tra diffractometer. The diffraction patterns were obtained in the  $2\theta$  range from 15° to 70° with a step of 0.05° using the Cu K $\alpha$  radiation ( $\lambda = 1.5418 \text{ \AA}$ ). The phases were identified using the powder diffraction database PDF-4+. The quantitative phase analysis was performed by the Rietveld method using the TOPAS program. The instrumental broadening was described with metallic

1  
2  
3  
4 silicon as a reference material. The coherent scattering region (CSR) was calculated using LVol-  
5  
6  
7 IB values (i.e. volume averaged column height calculated from the integral breadth).  
8  
9

10 The chemical composition of the oxides was analyzed by X-ray absorption near edge structure  
11  
12 (XANES) spectroscopy. The experiments were performed at the P65 beamline <sup>35</sup> at the  
13  
14 synchrotron radiation facility PETRA III (DESY, Hamburg, Germany). The electron storage ring  
15  
16  
17 of PETRA III was operating at 6 GeV in the top-up mode keeping the electron current stable within  
18  
19  
20 1%. The synchrotron radiation was provided by an 11-period undulator. The radiation was  
21  
22  
23  
24 monochromatized using a water-cooled double-crystal monochromator with Si(111) and Si(331)  
25  
26  
27 single crystal pairs. The powdered sample was pressed between two Kapton® films. The Co and  
28  
29  
30 Mn K-edge XANES spectra were recorded in the transmission mode using ionization chambers.  
31  
32  
33  
34 The XANES data were processed according to standard procedures with the ATHENA program  
35  
36  
37 of the IFEFFIT software package <sup>36</sup>.  
38  
39  
40  
41  
42  
43

44 The temperature-programmed reduction in hydrogen (TPR-H<sub>2</sub>) was performed with 40-60 mg  
45  
46  
47 of a sample in a quartz reactor using a flow setup with a thermal conductivity detector. The  
48  
49  
50 reducing mixture contained 10 vol.% of H<sub>2</sub> in Ar was passed through the setup with a constant  
51  
52  
53  
54  
55  
56  
57  
58  
59  
60



1  
2  
3  
4 flow rate near 40 ml/min. The rate of heating from room temperature to 900 °C was approximately  
5  
6  
7 10°C/min.  
8  
9

10 *In situ* XRD experiments were also performed at the P65 beamline. The reduction was studied  
11  
12  
13 under a flow 10% H<sub>2</sub> in helium with the flow rate of 10 mL/min. The sample was loaded into a  
14  
15  
16 quartz capillary, allowing gas to pass through the sample volume. The capillary temperature was  
17  
18  
19 increased from 25 to 600 °C with a heating rate of 10°C/min using a calibrated gas blower. The  
20  
21  
22 energy of synchrotron radiation was 20 keV, the beam size was 1.0 mm × 1.2 mm. XRD patterns  
23  
24  
25 were recorded using an XSpecrtrum Lambda 750k detector. The accumulation time was 1 min per  
26  
27  
28  
29  
30 scan. Corundum was used as a standard.  
31  
32

33  
34 In addition, the reduction of the *Mn<sub>2.5</sub>Co<sub>0.5</sub>* sample was studied by XPS. The experiments were  
35  
36  
37 performed using an X-ray photoelectron spectrometer (SPECs Surface Nano Analysis GmbH,  
38  
39  
40 Germany) equipped with an XR-50M X-ray source, a FOCUS-500 X-ray ellipsoidal  
41  
42  
43 monochromator, a PHOIBOS-150 hemispherical electron energy analyzer, and a high-pressure  
44  
45  
46 cell (HPC). To elucidate the reduction process, the sample was treated in hydrogen at 150, 250,  
47  
48  
49 300, and 400 °C. Each treatment was performed in the HPC at atmospheric pressure for 30 min.  
50  
51  
52  
53  
54 After the treatment, the sample was cooled to room temperature, the HPC was pumped out, and  
55  
56  
57  
58  
59  
60

the sample was transferred to the analytical chamber without contact with air, where the  $\text{Co}2p$ ,  $\text{Mn}2p$ ,  $\text{C}1s$ , and  $\text{O}1s$  core-level spectra were recorded under ultrahigh vacuum conditions. This allowed us to “freeze” a reduced state formed after the treatment at atmospheric pressure and to study in detail the reduction process using the convenient XPS apparatus. This approach is referred to as a pseudo in situ XPS study<sup>37</sup>. The core-level spectra were obtained using the monochromatic Al  $\text{K}\alpha$  radiation ( $h\nu = 1486.74 \text{ eV}$ ). The charge correction was performed by setting the  $\text{C}1s$  peak at 284.8 eV. Relative concentrations of elements were determined from the integrated intensities of the core-level spectra using the cross sections according to Scofield<sup>38</sup>. For detailed analysis, the spectra were fitted into several peaks after the background subtraction by the Shirley method. The fitting procedure was performed using the CasaXPS software<sup>39</sup>. The line shape of the peaks was approximated by the multiplication of the Gaussian and Lorentzian functions.

### 3. RESULTS

**Structure and Chemistry of As-prepared Samples.** Figure 1a shows X-ray diffraction patterns of  $\text{Mn}_x\text{Co}_{3-x}$  with  $x$  varying from 0.1 to 2.9. For  $x = 0.1$ , the XRD pattern corresponds to  $\text{Co}_3\text{O}_4$ -like oxide with the cubic spinel structure [space group  $Fd\bar{3}m$ , PDF No 00-043-1003]. With an increase in the Mn content, the diffraction reflections broaden and shift toward the lower angular

region. For  $x = 1.3$ , the XRD pattern exhibits additional peaks at  $2\theta = 29.3^\circ$ ,  $31.1^\circ$ ,  $33.2^\circ$ ,  $44.8^\circ$ ,  $52.2^\circ$ , and  $60.8^\circ$ , which belong to the tetragonal spinel of the  $\text{Mn}_3\text{O}_4$ -type structure [space group  $I4_1/amd$ , PDF No 00-024-0734]. For  $x = 1.3$ -1.7, a two-phase pattern is observed. The phase quantification by the Rietveld refinement is shown in Figure 1b. As seen, an increase in the Mn content leads to a gradual decrease in the amount of the cubic phase and an increase in the tetragonal oxide content. For  $x > 1.7$ , the diffraction patterns exhibit only reflections of the tetragonal phase of the  $\text{Mn}_3\text{O}_4$  type (Figure 1a).

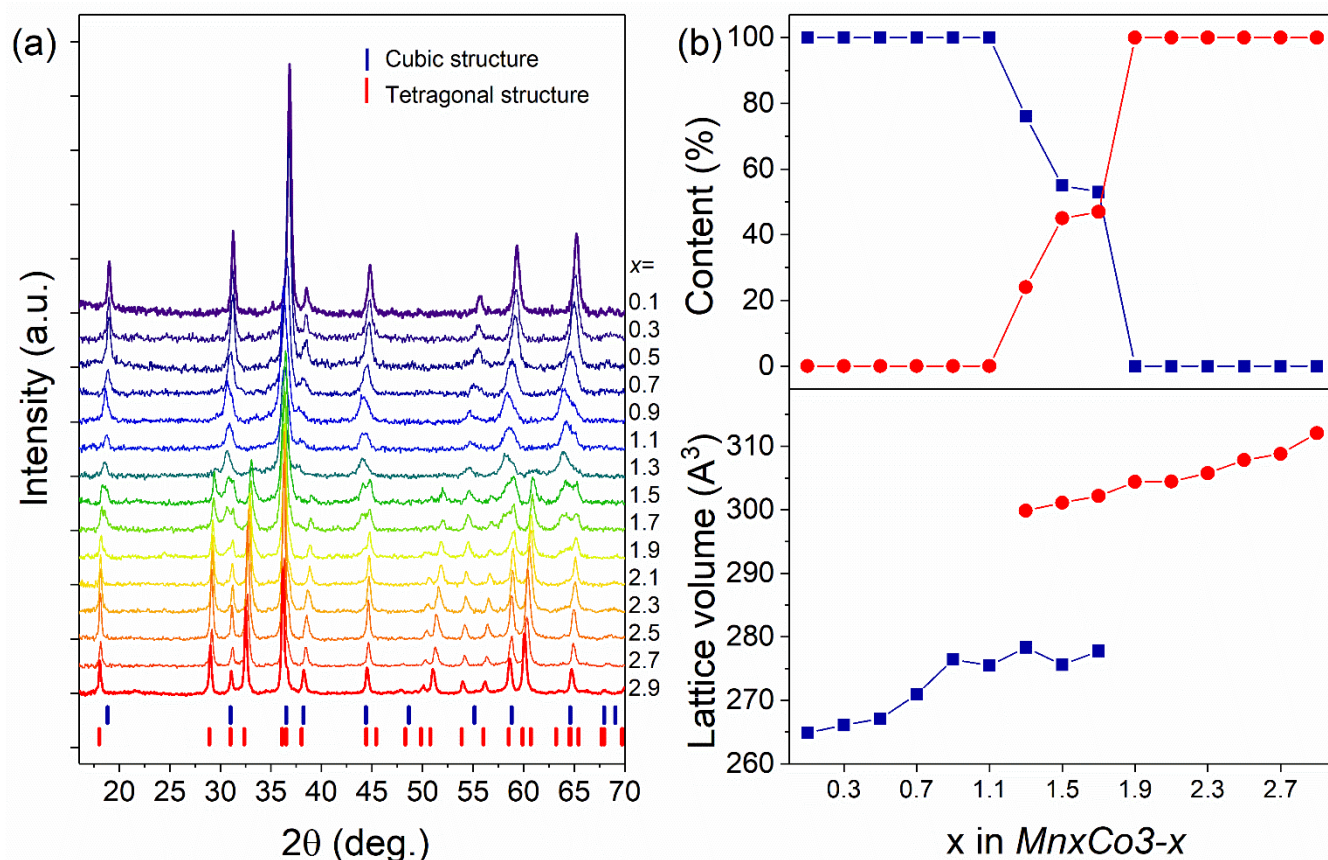


**Figure 1.** XRD patterns of the  $MnxCo3-x$  samples (a); the red bar chart indicates the reflections of tetragonal spinel [ $Mn_3O_4$ , PDF No 00-024-0734], the blue bar chart indicates cubic spinel [ $Co_3O_4$ , PDF No 00-043-1003]. Normalized lattice volume, content of cubic (blue squares) and tetragonal (red circles) spinels in dependence on the Mn content ( $x$ ) in  $MnxCo3-x$  sample (b).

As known,  $Co_3O_4$  has the structure of cubic spinel with the  $Fd\bar{3}m$  space group and is characterized by 8 formula units, while  $Mn_3O_4$  forms the tetragonal spinel ( $I4_1/amd$ ), which contains 4 formula units. Since the structures of tetragonal and cubic spinels contain a different number of formula units, for a convenient comparison of the lattice parameters of mixed oxides, we used the normalized volume  $V^*$  of the unit cell. For the cubic oxide, the volume is calculated as  $V^* = a^3/2$ , and for the tetragonal oxide, the volume is calculated as  $V^* = a^2 c$ . Figure 1b shows the normalized volume for the mixed Mn-Co oxides in dependence on the Mn content ( $x$ ) in sample. As seen, the normalized lattice volume gradually increases with increasing  $x$  from 0.1 to 0.9. In the range of  $x$  from 1.3 to 1.7, the volume changes sharply, which is associated with the appearance of the tetragonal phase. Since the ionic radius of manganese is larger than that of cobalt ( $r = 0.58 \text{ \AA}$ , CN = 6 for  $Mn^{3+}$ ,  $r = 0.55 \text{ \AA}$ , CN = 6 for  $Co^{3+}$ ;  $r = 0.56 \text{ \AA}$ , CN = 4 for  $Co^{2+}$  <sup>40</sup>), the increase in the normalized volume indicates the incorporation of manganese into the oxide

structure with the formation of solid solutions. From  $x = 0.1$  to  $x = 0.9$ , manganese cations are gradually introduced into the  $\text{Co}_3\text{O}_4$  structure. For  $x = 0.9$ -1.7, the change in the cubic lattice volume is insignificant, and  $V^* = 276.3$ -278.3  $\text{\AA}^3$  (Table S1), which is close to value for the  $\text{Co}_2\text{MnO}_4$  oxide ( $V^* = 282.7 \text{ \AA}^3$  for  $\text{Co}_2\text{MnO}_4$  [PDF No 00-023-1237]). From  $x = 1.3$  to  $x = 2.9$ , the volume of the tetragonal phase increases from 299.9 to 311.9  $\text{\AA}^3$ , which corresponds to an increase in the concentration of manganese cations in the solid solution. The increase in  $x$  is accompanied by a gradual decrease in the CSR of the cubic oxide from 220 to 80  $\text{\AA}$  and by an increase in the CSR of the tetragonal phase from 100 to 260  $\text{\AA}$  (Table S1). With the addition of a dopant, the microstrains increase from 0.12% to 0.45% and from 0.04% to 0.17% for cubic and tetragonal oxides, respectively. During the formation of solid solutions, an increase in microstrains is observed due to the difference in the atomic radii of the elements. In fact, geometrically different atoms are located in crystallographically equivalent positions, which leads to deformations. An increase in stresses leads to a loss of long-range order in the arrangement of atoms, and thus to decrease in the CSR.

During the formation of solid solutions, a change in the crystalline size of particles often occurs in comparison with simple oxides. The introduction of the second element can lead to a change in

1  
2  
3  
4 microstructural characteristics, both due to interaction at the atomic level, i.e. the formation of  
5  
6  
7 solid solutions, and mechanically preventing, for example, the crystallization of the compound  
8  
9  
10 when the modifier is in the form of individual particles or within the grain boundaries.  
11

12  
13 The Mn K-edge XANES spectra of the  $MnxCo3-x$  samples for  $x = 0.1, 0.3, 0.7, 1.1, 1.9, 2.3,$   
14  
15  
16  
17 2.5, and 2.7 (Figure 2a) as well as the spectra of standard Mn-based materials (Figure 2b) were  
18  
19  
20 obtained to elucidate the chemical state of manganese cations in the mixed oxides. The Mn K-edge  
21  
22  
23 XANES spectra contain two regions: the main peak of the K-edge absorption due to the  $1s \rightarrow 4p$   
24  
25  
26 transition (peak C in Figure 2a) and the pre-edge region (peaks  $A_1$  and  $A_2$  in Figure 2a) due to the  
27  
28  
29  $1s \rightarrow 3d$  transitions, which represent electronic and structural features. At the absorption edge, the  
30  
31  
32 inflection point contains a shoulder (B). As shown in the inset in Figure 2a, the pre-edge region is  
33  
34  
35 characterized by a splitting of 3d orbitals into  $t_{2g}$  and  $e_g$  orbitals. The relative increase in the  $A_2$   
36  
37  
38 peak intensity indicates an increase in the number of unoccupied  $e_g$  orbitals in the  $1s \rightarrow 3d$   
39  
40  
41 quadrupole-allowed transition, which is in agreement with the increased  $Mn^{4+}/Mn^{3+}$  ratio in the  
42  
43  
44 manganese oxides<sup>41, 42</sup>.  
45  
46  
47  
48  
49  
50  
51  
52  
53  
54  
55  
56  
57  
58  
59  
60

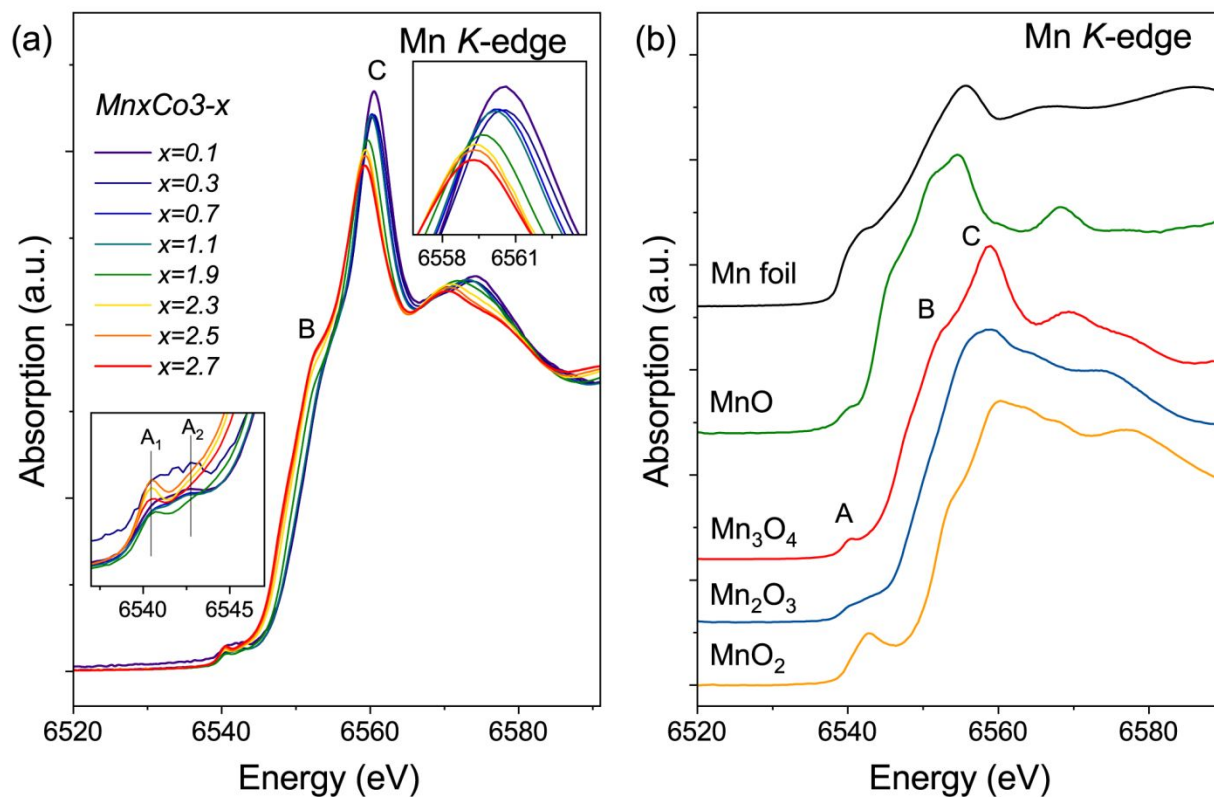


**Figure 2.** Normalized Mn *K*-edge XANES spectra of the  $Mn_xCo_{3-x}$  samples for  $x = 0.1, 0.3, 0.7, 1.1, 1.9, 2.3, 2.5,$  and  $2.7$  (a) and  $MnO_2, Mn_2O_3, Mn_3O_4, MnO,$  and  $Mn$  foil (b).

The Mn absorption edge of the  $Mn_xCo_{3-x}$  samples with  $x = 2.7-2.3$  is similar to that of  $Mn_3O_4$ . The shift of the absorption edge toward that of  $MnO_2$  with decreasing  $x$  shows that Mn is further oxidized during the substitution of Mn by Co. Simultaneously, the intensity of the  $A_2$  peak in the pre-edge region (the inset in Figure 2a) decreased slightly with increasing  $x$  in the  $Mn_xCo_{3-x}$  samples, indicating the reduction of  $Mn^{4+}$  cations to  $Mn^{3+}$ .

XANES is an effective tool for determining the average oxidation states of an absorbing element in a sample<sup>43, 44</sup>. It is known that the main edge shifts to higher energies with an increase in the oxidation state of Mn. There is a nearly linear relationship between edge-energy positions and formal oxidation state of Mn in the series of Mn-oxides. XANES edge-energy varies by a few electron volts from sample to sample, in part because it depends on oxidation state averaged for all the Mn atoms in the sample.<sup>45</sup> Besides, ligands bound to the absorbing element also contribute to the general shape of the edge and apparent edge energy.<sup>46, 47</sup> As a result, this correlation between edge-energy and an element's formal oxidation state is purely empirical and definition of the specific oxidation state of the element at each site is complicated.<sup>48, 49</sup>

The Mn K-edge XANES spectra of bulk manganese oxides (Figure 2b) were used to determine the correlation between the absorption edge position and the oxidation state of manganese. Figure 3 shows a linear dependence of the oxidation state of Mn on the position of the K-edge in the series of manganese oxides: MnO (Mn<sup>2+</sup>), Mn<sub>3</sub>O<sub>4</sub> (Mn<sup>2.66+</sup>), Mn<sub>2</sub>O<sub>3</sub> (Mn<sup>3+</sup>), and MnO<sub>2</sub> (Mn<sup>4+</sup>)<sup>50-55</sup>. The absorption edge of manganese in the metallic state is at 6539 eV<sup>56</sup>. The absorption edge for the *MnxCo3-x* oxides shifts with the Mn content (Figure 3, red circles).



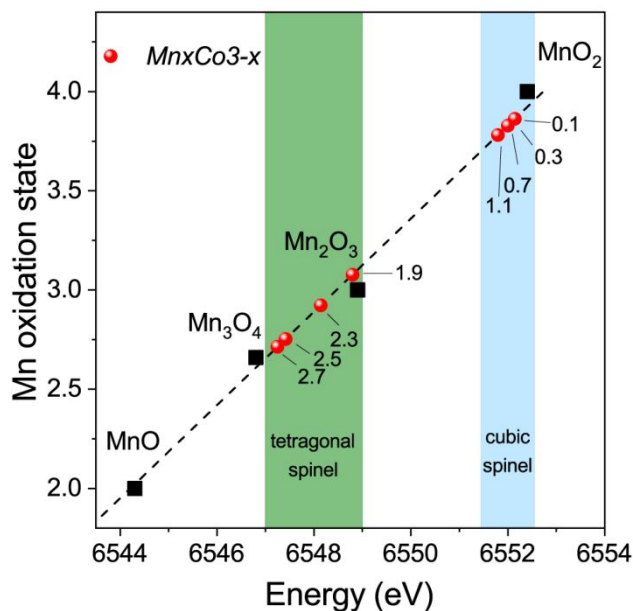


**Figure 3.** Calibration curves for XANES analysis determined using manganese oxides as references. Red circles indicate experimental data for the  $Mn_xCo_{3-x}$  samples (numbers near the red circles indicate the value of  $x$ ). Black squares correspond to reference oxides.

The absorption edge of the  $Mn_{2.7}Co_{0.3}$  sample at  $E = 6547.25$  eV corresponds to the charge state of  $2.71+$ . With a decrease in the Mn content from  $x = 2.7$  to  $x = 1.9$ , the energy of the absorption edge increases to  $6548.80$  eV, corresponding to Mn in the charge state of  $3.08+$ . With a further decrease in the manganese content, the space group changes from tetragonal  $I4_1/amd$  ( $x = 2.7-1.9$ ) to cubic  $Fd\bar{3}m$  ( $x = 1.1-0.1$ ). As seen, the absorption edge sharply shifts from  $6548.80$  eV ( $x = 1.9$ ) to  $6551.80$  eV ( $x = 1.1$ ). Hence, we can speculate that the average oxidation states for

the cubic oxides are higher than that for the tetragonal modification. According to the calibration curve, a decrease in  $x$  from 1.1 to 0.1 leads to a growth of the oxidation state of Mn cations from 3.78+ to 3.86+.

The Co K-edge XANES spectra are shown in Figure 4. In the case of  $Mn_xCo_{3-x}$  ( $x = 0.1-1.1$ ), the spectra have similar shape to  $Co_3O_4$ , and cobalt cations have the oxidation state near 2.6+.<sup>57</sup> When the Mn content increases from 1.1 to 2.7, the main peak of the XANES spectra shift from 7729 to 7731.7 eV 7731.5 to 7731.0 eV and its intensity gradually decreases, indicating a lower oxidation state of Co at a lower Co content. Similar results have been obtained in other spinel Co-Mn system.<sup>50</sup> A lower Co valence value tends to appear in oxides with lower Co content, suggesting an increase in the ratio of  $Co^{2+}/Co^{3+}$  due to substitution of Mn cations.<sup>58</sup> The Co K-edge XANES spectra exhibit some changes in the shape of the edge as Co is substituted by Mn due to changes in the local environment of Co. However, they do not show a steady shift to lower energies when the Mn content increases from 0.1 to 1.1 and then from 1.9 to 2.7. Because the energy shift is below 1 eV when  $x$  changes in the ranges of 0.1-1.1 and 1.9-2.7, the estimated difference between the oxidation states of cobalt is less than 0.1.<sup>10</sup> However, unlike the shift in the Mn K-edge XANES spectra, a shift of the main absorption peak in the Co K-edge spectra

toward lower energies ( $\approx 1.0$  eV) is evident when  $x$  increases from 1.1 to 1.9. This behavior can be explained as due to local environment of cobalt. Cobalt occupies cubic and tetrahedral positions in cubic spinel structure in the case of  $MnxCo_{3-x}$  ( $x = 0.1-1.1$ ), while it occupies mainly tetrahedral positions in tetragonal spinel ( $x = 1.9-2.7$ ).

For pure  $Mn_3O_4$  and  $Co_3O_4$ , the average oxidation state of cations is 2.66+. For the tetragonal solid solutions ( $x = 1.9-2.7$ ), the oxidation state of Mn is between 2.71+ and 3.08+, which is close to the theoretical value of 2.7-3 (the theoretical average oxidation state of Mn is calculated from the electroneutrality principle and assumption that  $Mn_xCo_{3-x}O_4$  oxide contains  $Co^{2+}$  cations for  $x \geq 2$ ). Unfortunately, the exact state of cobalt is difficult to determine. For  $x < 1.1$ , a cubic spinel is formed, in which the average oxidation state of Mn is greater than 3+. Probably, Mn is partially in the  $Mn^{4+}$  state, which is in a good agreement with the literature data for Mn-Co oxide solid solutions <sup>59</sup>.

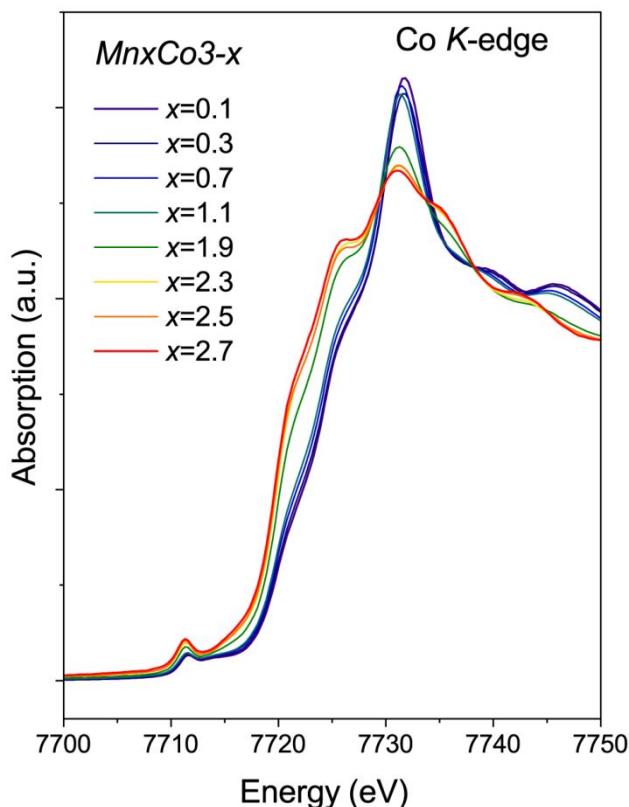
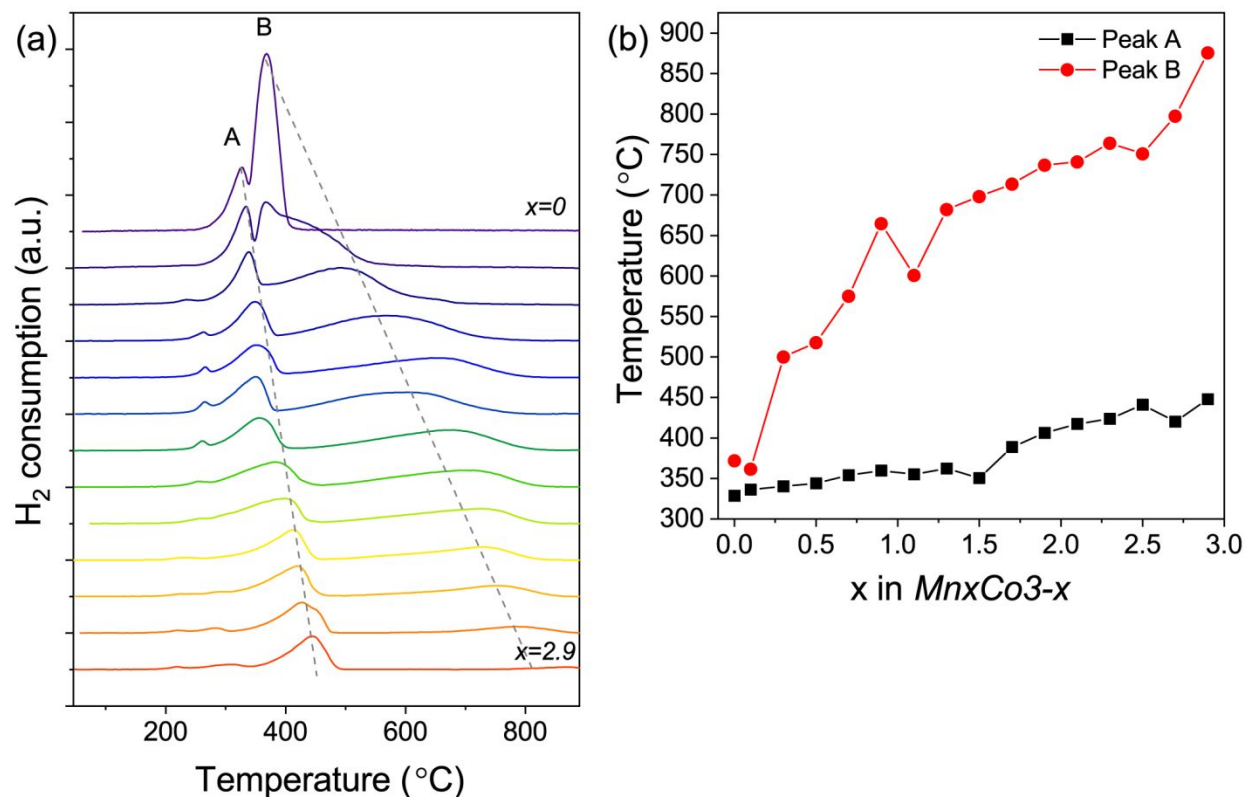


**Figure 4.** Co *K*-edge XANES spectra of the  $Mn_xCo_{3-x}$  samples for  $x = 0.1, 0.3, 0.7, 1.1, 1.9, 2.3, 2.5$ , and  $2.7$ .

**TPR- $H_2$  Study.** Figure 5a shows TPR curves for  $Mn_xCo_{3-x}$  with  $x$  varying from 0.1 to 3. As seen, the TPR curve of pure  $Co_3O_4$  ( $x = 0$ ) exhibits two peaks of hydrogen consumption with maxima at 320 °C (A peak) and 370 °C (B peak). The presence of two peaks corresponds to the two-step reduction:  $Co_3O_4 + H_2 \rightarrow 3CoO + H_2O$  and  $CoO + H_2 \rightarrow Co + H_2O$ <sup>21,60</sup>. With an increase

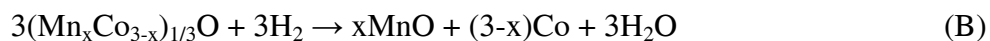
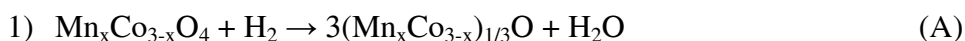
in x and with the incorporation of manganese cations into the oxide structure, the following three effects are observed on the TPR curves.

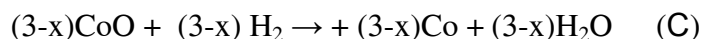
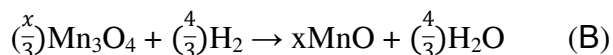
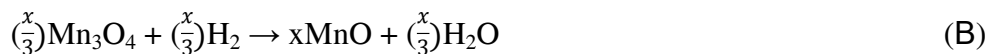
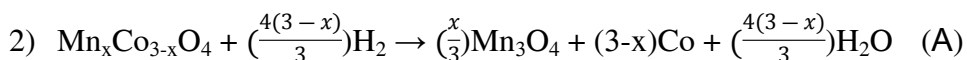
- (1) The A peak shifts from 320 to 450 °C, and the B peak shifts from 370 to 875 °C (Figure 5b).
- (2) The ratio of the peak intensities changes. The hydrogen consumption increases for the A peak and decreases for the B peak (Figure 5a). The total amount of consumed hydrogen decreases from 17.3 to 5.33 mmol H<sub>2</sub>/g due to the reduction of cobalt oxide to Co<sup>0</sup> and manganese oxide to Mn<sup>2+</sup>.
- (3) There appear small low-temperature peaks. Probably, they are associated with the reduction of amorphized or highly dispersed oxides, which are undetectable by XRD.



**Figure 5.** TPR-H<sub>2</sub> profiles of  $Mn_xCo_{3-x}$  samples with  $x$  increasing from 0 to 2.9 (a). Position of A and B peaks in dependence on the Mn content (b).

The following reaction pathways of the reduction of  $Co_{3-x}Mn_xO_4$  can be considered: (1) the reaction proceeds through the formation of the mixed oxide  $(Mn_xCo_{3-x})_{1/3}O$ , (2) the release of Co from the structure of the  $Co_{3-x}Mn_xO_4$  solid solution, (3) the formation of CoO.





All the proposed reaction routes are characterized by two or three stages, indicating that there are several peaks of the hydrogen consumption on the TPR curves. The intensity of A and B (C) peaks depends on  $x$  and the reaction route. Figure 6 illustrates a theoretical dependence of the relative amount of the hydrogen consumption at stage A on the Mn content  $x$  (the ratio between the integrated peak area of the A peak and the total amount of consumed hydrogen). For the 1<sup>st</sup> reaction route, the consumption at stage A rises with increasing  $x$ . In the case of the 2<sup>nd</sup> and 3<sup>rd</sup> pathways, another dependence is observed: the amount of hydrogen for stage A declines with an increase in  $x$ . The experimental data are also shown in Figure 6 (blank hexagons). As seen, the experimental dependence agrees well with the first reaction route, i.e., the reduction of a solid solution proceeds through the formation of the  $(\text{Mn}_x\text{Co}_{3-x})_{1/3}\text{O}$  intermediate. To confirm these

assumptions further, we applied *in situ* XRD and XPS techniques to study the chemical state of cations and the crystal structure of Mn-Co oxide solid solutions under a hydrogen flow.

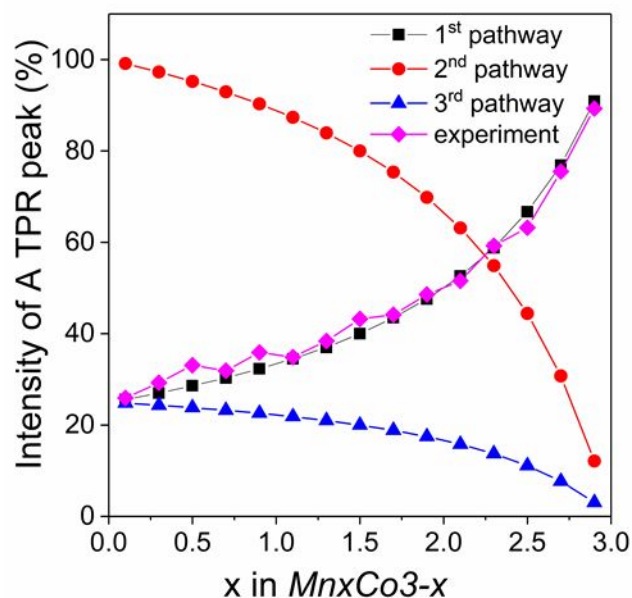
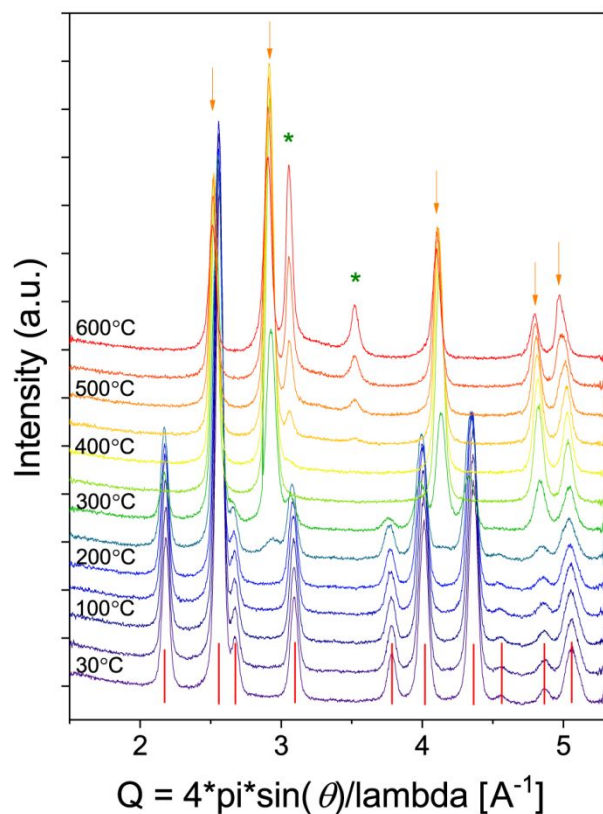


**Figure 6.** Relative intensity of the A peak in dependence on Mn content ( $x$ ) in  $Mn_xCo_{3-x}$  for three theoretical reaction pathways (squares – 1<sup>st</sup>, circles – 2<sup>nd</sup>, triangles – 3<sup>rd</sup> and diamonds – experimental data)

***In Situ* XRD Study.** The phase transformations that occur during the reduction of  $Mn_xCo_{3-x}$  have been further studied by *in situ* XRD (Figure 7, Figures S1-S5). In these experiments, the XRD patterns were collected during heating the samples in the  $H_2/He$  mixture from room temperature to 600 °C with a ramp of 10°C/min. The results of the investigation of  $Mn_{0.7}Co_{2.7}$  are presented



in Figure 7. At room temperature, the sample consists of cubic spinel  $\text{Mn}_{3-x}\text{Co}_x\text{O}_4$ . At 250 °C, the intensity of spinel reflections declines, and wide peaks appear at  $Q = 2.56, 2.91, 4.12, 4.80, 4.97 \text{ \AA}^{-1}$ , which correspond to reflections of a (Co,Mn)O-like oxide [CoO, PDF No 00-042-1300]. At 450 °C, new peaks appear at  $Q = 3.06$  and  $3.51 \text{ \AA}^{-1}$ , which are attributed to 111 and 200 reflections of metallic cobalt (fcc) [Co, PDF No 00-015-0806], and the intensity of a (Co,Mn)O-like intermediate compound decreases. At 450–600 °C, there appear reflections of metallic Co and the (Co,Mn)O-like oxide.



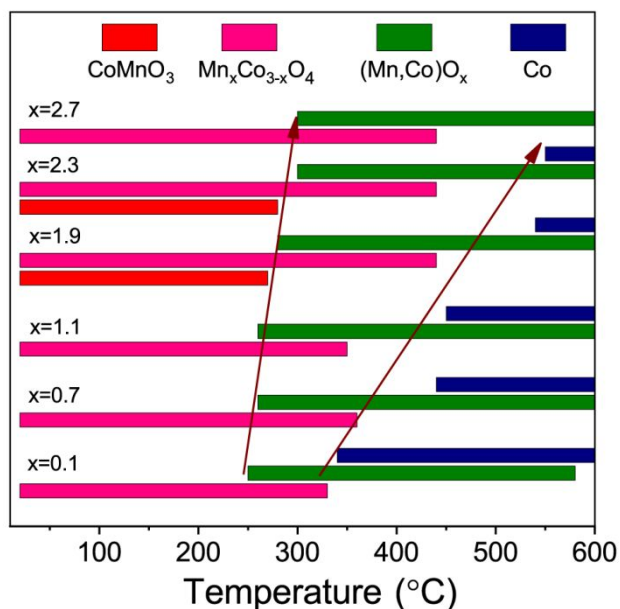
**Figure 7.** *In situ* XRD patterns of  $Mn_{0.7}Co_{2.3}$  collected during heating from 30 to 600 °C in a flow of 10%  $H_2$  in He gas mixture. Lines indicate the position of  $Mn_{3-x}Co_xO_4$  cubic spinel reflections, arrows indicate the (Co,Mn)O-like oxide, and the asterisks indicate Co in the metallic state.

Figure 8 summarizes the results of the *in situ* XRD data and shows the temperature ranges for the existence of different phases during the reduction of  $Mn_xCo_{3-x}$  samples with  $x = 0.1, 0.7, 1.1, 1.9, 2.3,$  and  $2.7$ . It is worth noting that for the samples with  $x = 1.9, 2.3$ , the  $CoMnO_3$  phase is observed in the initial state (14 wt % and 5 wt % for  $x = 1.9$  and  $2.3$ , respectively). Reflections of this phase are undetectable with the laboratory diffractometer (Figure 1a) because of insufficient intensity of the incident beam, in contrast to the synchrotron radiation. During the reduction,  $CoMnO_3$  disappears at 270-300 °C. All the compositions undergo the following transformations:

$$Mn_xCo_{3-x}O_4 \rightarrow (Mn_xCo_{3-x})_{1/3}O \rightarrow Co + MnO.$$

With an increase in the Mn content from  $x = 0.1$  to  $x = 2.7$ , the formation temperature of the intermediate oxide (Mn,Co)O rises from 250 to 300 °C. In addition, the rise in  $x$  from 0.1 to 2.3 leads to an increase in the formation temperature of metallic cobalt from 340 to 550 °C. These results are in good agreement with the TPR data (Figure 6). The

addition of Mn slows down the transformations in the initial spinel and stabilizes the intermediate compound (Mn, Co)O oxide.



**Figure 8.** Phase composition of  $Mn_xCo_{3-x}$  ( $x = 0.1, 0.7, 1.1, 1.9, 2.3$ , and  $2.7$ ) as a function of reduction temperature.

The TPR and *in situ* XRD data testify to a two-stage reduction process through the formation of an intermediate compound  $(Mn_xCo_{3-x})_{1/3}O$ , which is consistent with our previous studies<sup>34</sup>. The gradual introduction of manganese cations into the cobalt oxide structure slightly increases the temperature of the first reduction step and strongly increases the temperature of the second step (the maximum of the first TPR peak shifts from 320 to 450 °C, whereas the maximum of the second

TPR peak shifts from 370 to 875 °C). The presence of Mn and Co cations in one oxide matrix significantly affects the second stage of reduction, but does not influence the first one. Apparently, this is due to the “similarity” of the structures of the initial spinels  $\text{Mn}_x\text{Co}_{3-x}\text{O}_4$  and  $\text{Co}_{1-x}\text{Mn}_x\text{O}$  (rock salt). The spinel consists of a close packing of oxygen, in which cations are located in octahedral and tetrahedral positions, while some of the «non-spinel» octahedral and tetrahedral sites remain empty. The rock salt structure also has a close packing of oxygen, in which cations are located in all octahedral voids. Therefore, for the rearrangement from  $(\text{Mn},\text{Co})_3\text{O}_4$  to  $(\text{Co},\text{Mn})\text{O}$ , it is necessary to move an atom from a tetrahedral position to a neighboring octahedral void. We have previously shown <sup>61</sup> that, during the initial stages of  $\text{Co}_3\text{O}_4$  reduction, cobalt cations fill the main and additional octahedral positions of spinel, i.e. three filled octahedra are formed, which means the formation of CoO clusters in the  $\text{Co}_3\text{O}_4$  structure. However, the  $\text{CoO} \rightarrow \text{Co}$  transformation requires a complete rearrangement of the structure: oxygen withdrawal, a decrease in the Co-Co distance, and redistribution of atoms. With the introduction of manganese, which retains oxygen more strongly than cobalt (standard electrode potentials are equal to -0.29 and -1.18 eV for  $\text{Co}^{2+}/\text{Co}^0$  and  $\text{Mn}^{2+}/\text{Mn}^0$ , respectively), the exit of cobalt cations from the structure becomes more difficult.

**Pseudo in Situ XPS Study.** Changes in the chemical state of cations in the *Mn<sub>2.5</sub>Co<sub>0.5</sub>* during the reduction by hydrogen were studied using *pseudo in situ* XPS. Table 1 shows relative concentrations (atomic ratios) of elements in the near-surface layer of the sample and the binding energies of Mn $2p_{3/2}$ , Co $2p_{3/2}$ , and O  $1s$  peaks. In the initial state, the atomic ratio [O<sup>\*</sup>]/[Mn + Co] is 1.22, which is close to the stoichiometric value of 1.3 for the spinel structure. During reduction, a gradual decrease in the oxygen content is observed.

**Table 1. Atomic ratios of elements, the binding energies of Mn $2p_{3/2}$ , Co $2p_{3/2}$ , and O  $1s$  peaks of *Mn<sub>2.5</sub>Co<sub>0.5</sub>* before and after reduction in hydrogen.**

Reduction temperature	[Co]/[Mn]	[O <sup>α</sup> ]/[Mn + Co]	Mn $2p_{3/2}$			Co $2p_{3/2}$		O $1s$
			Mn <sup>2+</sup>	Mn <sup>3+</sup>	Mn <sup>4+</sup>	Co <sup>0</sup>	Co <sup>2+</sup>	
fresh	0.128	1.22	640.1	641.5	642.6	–	780.5	529.9 <sup>α</sup>
			(14%)	(68%)	(18%)			531.5 <sup>β</sup>
150 °C	0.154	1.01	640.1	641.5	642.6	–	780.6	529.8 <sup>α</sup>
			(21%)	(67%)	(12%)			531.4 <sup>β</sup>
250 °C	0.200	0.78	640.1	641.6	–	–	780.5	529.6 <sup>α</sup>
			(52%)	(48%)				531.4 <sup>β</sup>
300 °C	0.177	0.81	640.1	641.6	–	–	780.6	529.6 <sup>α</sup>

			(53%)	(47%)				531.4 <sup>β</sup>
			640.1	641.5		778.0	780.4	529.6 <sup>α</sup>
400 °C	0.111	0.75			—			
			(55%)	(45%)		(35%)	(65%)	530.9 <sup>β</sup>

<sup>α</sup> oxygen characterized by the O1s binding energy at 529.6-529.9 eV corresponded to the mixed oxide;

<sup>β</sup> oxygen corresponded to the OH-groups.

Figure 9a shows the Mn2*p* core-level spectra of the *Mn2.5Co0.5* samples obtained before and after reduction in hydrogen at different temperatures. The shape of Mn2*p* spectra of fresh sample and high binding energy of Mn2*p*<sub>3/2</sub> peak indicate that manganese in the sample is in the oxidized state. Moreover, analysis of the Mn2*p* core-level spectrum allow us to reveal that manganese presences in the Mn<sup>2+</sup>, Mn<sup>3+</sup>, and Mn<sup>4+</sup> states. Indeed, to identify the chemical state of manganese, the binding energy of Mn2*p*<sub>3/2</sub> peak, the presence and position of shake-up satellites are used <sup>62-66</sup>. It should be mentioned that there is approach to fit the Mn2*p*<sub>3/2</sub> peak of individual manganese oxides by several peaks corresponded to Mn cations in the different coordinations and oxide states<sup>67 63</sup>. To study the reduction of Mn cations we applied the alternative approach – based on our experience of studying the Mn oxides synthesized in the similar conditions and characterized by the other methods we have constructed the peak fitting model for each individual oxide (not presented in this work) and then used the mix of the peak fitting models for fitting the Mn spectra

of samples under study. It allows us to reveal the trend concerning to reduction of Mn cations. The curve-fit analysis of the Mn $2p$  spectra of fresh sample shows that the spectrum is described by three Mn $2p_{3/2}$ -Mn $2p_{1/2}$  doublets and shake-up satellites, which indicates that the as-prepared sample contains Mn $^{2+}$ , Mn $^{3+}$ , and Mn $^{4+}$  cations (Figure 9a). According to the literature data, manganese in MnO, Mn $_2$ O $_3$ , and MnO $_2$  is characterized by the Mn $2p_{3/2}$  binding energy in the ranges of 640.4–641.7, 641.5–641.9, and 642.1–642.6 eV and the spin-energy splitting ( $\Delta E$ ) of Mn $3s$  core-level spectrum is 5.9-6.1, 5.2-5.3, and 4.5-4.7 eV, respectively <sup>62-66</sup>. The spin-energy splitting ( $\Delta E$ ) of Mn $3s$  core-level spectrum for fresh sample is 5.5 eV, that lies between ones corresponded to Mn $^{2+}$  and Mn $^{3+}$  cations. The XPS analysis allows us to estimate the fraction of Mn $^{2+}$ , Mn $^{3+}$ , and Mn $^{4+}$  cations for fresh sample that is 14%, 68%, and 18%, respectively (Table 1). The presence of Mn $^{4+}$  is likely associated with the oxidation of manganese in the near-surface layers or with the formation of highly dispersed CoMnO $_3$  <sup>68</sup>. After heating in hydrogen at 150 °C, manganese undergoes partial reduction and the fraction of manganese in the Mn $^{3+}$  and Mn $^{4+}$  states decreases (Table 1) and the spin-energy splitting ( $\Delta E$ ) of Mn $3s$  core-level spectrum increases to 5.6 eV as well. At 250-400 °C, the Mn $2p$  doublet, which could be attributed to manganese in the Mn $^{4+}$  state, does not appear in the spectra, while the fraction of manganese in the Mn $^{2+}$  + state

increases to 55%. And it should be noted that the spin-energy splitting ( $\Delta E$ ) of Mn3s core-level spectrum reaches to 5.9-6.0 eV that lies between ones corresponded to Mn<sup>2+</sup> and Mn<sup>3+</sup> cations but it is more closely to the Mn<sup>2+</sup> state.

The Co2p core-level spectra of *Mn2.5Co0.5* obtained before and after reduction in hydrogen are presented in Figure 9b. The spectra consist of the Co2p<sub>3/2</sub>-Co2p<sub>1/2</sub> doublet and corresponded “shake-up” satellites. In case of sample treated in hydrogen at 400°C there is additional Co2p<sub>3/2</sub>-Co2p<sub>1/2</sub> doublet with lower Co2p<sub>3/2</sub> binding energy. To identify the chemical state of cobalt, the position of the Co2p<sub>3/2</sub> main line, the shape of the Co2p spectrum (the intensity and relative position of the “shake-up” satellites), and the spin-orbit splitting Co2p<sub>3/2</sub>-Co2p<sub>1/2</sub> should be used<sup>69</sup>. In the case of *Mn2.5Co0.5*, the Co2p<sub>3/2</sub> spectra are represented by an asymmetric peak with a binding energy in the range of 780.4–780.6 eV and a broad “shake-up” satellite at 786.6 eV. The spin-orbit splitting of Co2p<sub>3/2</sub>-Co2p<sub>1/2</sub> is 15.95 eV. In the spectrum of metallic cobalt Co and the LiCoO<sub>2</sub> and Co<sub>3</sub>O<sub>4</sub> oxides, the “shake-up” satellites are not observed, and the Co2p<sub>3/2</sub> binding energy lies in the range of 778.0–778.2 and 779.5–780.5 eV<sup>63, 69, 70</sup>. Cobalt in the Co<sup>2+</sup> state is characterized by Co2p<sub>3/2</sub> binding energies in the range of 780.0–782.0 and by the presence of an intense “shake-up” satellite in the range of 786–787 eV<sup>69, 71</sup>. The Co2p<sub>3/2</sub> binding energy, as well



as the presence of distinct “shake-up” satellites, indicates that cobalt in the  $Mn_{2.5}Co_{0.5}$  sample is in the  $Co^{2+}$  state both initially and during reduction. The additional  $Co2p_{3/2}$ – $Co2p_{1/2}$  doublet with the  $Co2p_{3/2}$  binding energy at 778.0 eV observed after reduction at 400 °C corresponds to cobalt in the metallic state. The fraction of metallic cobalt is about 35%.

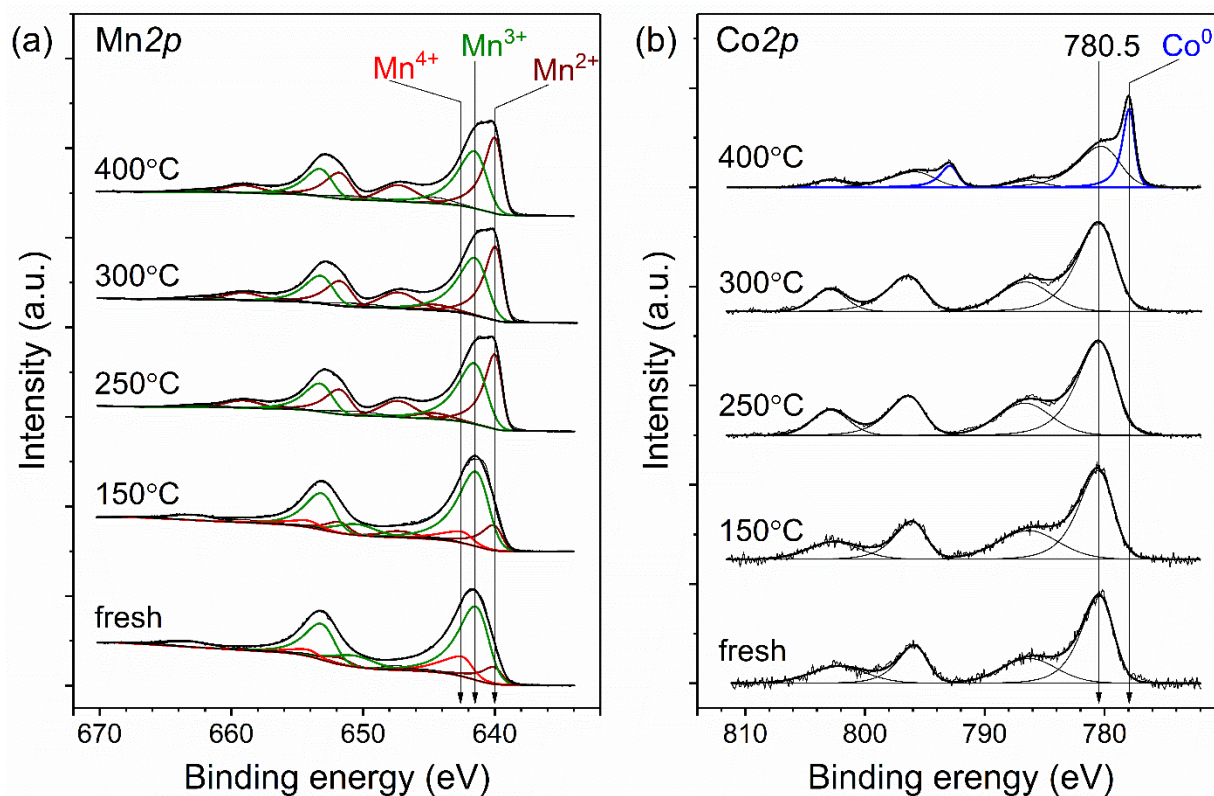


**Figure 9.** Mn2p (a) and Co2p (b) core-level spectra of the  $Mn_{2.5}Co_{0.5}$  samples obtained before and after reductive treatment in hydrogen. The Co2p spectra are normalized to the integrated intensity of the corresponding Mn2p spectra.

During the reduction at temperatures up to 250 °C, the surface cobalt content gradually rises and the [Co]/[Mn] ratio increases from 0.128 to 0.200. In contrast, at 250-400 °C, the ratio decreases to 0.111. Apparently, cobalt ions diffuse into the bulk of the solid solution, despite the fact that, according to the *in situ* XRD and TPR results, the formation of (Mn,Co)O is observed in this temperature range. At 400 °C, the surface content of Co<sup>2+</sup> begins to decrease and metallic cobalt appears, which obviously indicates the formation of Co<sup>0</sup> clusters on the oxide surface.

The behavior of Mn is more complicated. During reduction at 250 °C, Mn<sup>4+</sup> cations completely disappear. With the further heating, the fraction of Mn<sup>3+</sup> decreases and the fraction of Mn<sup>2+</sup> increases. The main peculiarity is that at 300-400 °C, the oxide surface contains about 50% of Mn<sup>3+</sup>, and its content does not change significantly. According to the XRD and TPR data, at 300-400 °C (Co,Mn)<sub>3</sub>O<sub>4</sub> transforms to (Co,Mn)O. From the formal point of view, (Co, Mn)O contains cations in the 2+ oxidation state. Therefore, it can be assumed that fragments of the initial spinel including Mn<sup>3+</sup> cations are still preserved on the surface. Perhaps, bulk reduction occurs, as it was observed previously for Co<sub>3</sub>O<sub>4</sub> <sup>61</sup>.

The study of Co-Mn oxide reducibility is strongly motivated by its application as a catalyst <sup>23-27, 29-33</sup>. Under reduction in hydrogen, cobalt oxide undergoes the following transformations: Co<sub>3</sub>O<sub>4</sub>

→ CoO → Co, while the reduction of manganese oxide leads to the transformation  $\text{Mn}_3\text{O}_4 \rightarrow \text{MnO}$  <sup>18, 19, 21, 60</sup>. The temperature and pathway of the transformations depend on the preparation method, support, crystallite size, and composition of the reducing mixture <sup>7, 21, 61</sup>. The interaction of manganese and cobalt oxides leads to the formation of the mixed oxides, whose behavior is different from for the behavior of a mixture of simple oxides. Morales et al. <sup>8</sup> found that  $\text{Co}_3\text{O}_4$  supported on  $\text{TiO}_2$  catalysts was reduced to a mixture of CoO and Co at 425 °C. The introduction of Mn retards the reduction of supported  $\text{Co}_3\text{O}_4$  particles. Latter authors <sup>32</sup> showed that, depending on the degree of interaction between manganese and cobalt in the oxide state, the reduction products exhibit different microstructural characteristics, which significantly affects their catalytic performance in the Fischer-Tropsch synthesis.

Our results are in line with the previous reports and indicate that introduction of manganese into cobalt oxide shifts the reduction temperature to a higher temperature region. At that, the growth of the Mn content results in an increase in temperature for both stages (Figure 8). The reducibility of oxides was studied by the TPR technique, which is a simple method to monitor the reduction process by using the amount of hydrogen that the sample adsorbs. It was demonstrated that TPR profiles of Mn-Co oxides change with a variation of the Mn:Co ratio <sup>27, 33</sup>. Qu et al. <sup>27</sup> showed that

interaction between Co and Mn oxides for Mn:Co < 1 leads to a shift of TPR profiles to higher temperature region compared to simple oxides, indicating the worsening of the reducibility. For Mn:Co > 1, the TPR profiles exhibit new low temperature peaks. Wu et al.<sup>33</sup> found that the TPR curves of Mn-Co oxides are ascribed to the reductions of MnO<sub>2</sub>/Mn<sub>2</sub>O<sub>3</sub> to Mn<sub>3</sub>O<sub>4</sub> and Co<sub>3</sub>O<sub>4</sub> to CoO, and the broad reduction peak at >500 °C can be attributed to the reduction of Mn<sub>3</sub>O<sub>4</sub> to MnO and CoO to Co. However, they found some effects, such as appearance of low- and high-temperature peaks, showing a strong synergistic effect between Co<sub>3</sub>O<sub>4</sub> and MnO<sub>x</sub>. It should be noted that during the synthesis, a mixture of different states is often formed (e.g. solid solutions based on cobalt and manganese oxide and simple oxides); therefore, there is a challenge to attribute the signal to the reduction of each compound. As a result, there is quite a lot of confusion in the literature with the interpretation of TPR results. Previously the mechanism of reduction of double oxides was investigated using a mixture of CoMn<sub>2</sub>O<sub>4</sub> and MnCo<sub>2</sub>O<sub>4</sub><sup>34</sup>, and it was shown that the reduction process strongly differs from that observed for simple oxides Co<sub>3</sub>O<sub>4</sub> and Mn<sub>3</sub>O<sub>4</sub> in spite of similar TPR profiles. Reduction of CoMn<sub>2</sub>O<sub>4</sub> and MnCo<sub>2</sub>O<sub>4</sub> proceeds through the formation of intermediate compounds Mn<sub>0.6</sub>Co<sub>0.4</sub>O and Co<sub>0.6</sub>Mn<sub>0.4</sub>O to MnO and metallic Co. The results of the reported work show that the reduction of Co<sub>3-x</sub>Mn<sub>x</sub>O<sub>4</sub> occurs in two stages. The gradual

introduction of manganese cations into the structure of cobalt oxide slightly increases the temperature of the first reduction step  $(\text{Mn,Co})_3\text{O}_4 \rightarrow (\text{Mn,Co})\text{O}$ . In contrast, the influence of the addition of Mn onto the second stage is quite significant: the temperature of the transformation  $(\text{Mn,Co})\text{O} \rightarrow \text{MnO} + \text{Co}$  shifts by ca. 500 °C. The presence of Mn and Co cations in the same spinel matrix significantly impairs oxide reducibility.

#### 4. CONCLUSIONS

A series of  $\text{Mn}_x\text{Co}_{3-x}$  samples with x varying from 0 to 2.9 was prepared by coprecipitation of cobalt and manganese nitrates with subsequent calcination at 600 °C in air. The initial oxides were characterized by XRD and XANES. The solubility limits of Mn and Co cations in the solid solution (spinel with a cubic or tetragonal structure) were determined. For x = 0.1-1.1, a solid solution is formed on the basis of the cubic spinel structure. For x = 1.3-1.7, there is a two-phase system consisting of cubic and tetragonal oxides, and for x = 1.9-2.9, a solid solution is formed on the basis of tetragonal spinel. The average oxidation state of manganese ions for the cubic oxide is higher (3.78+ - 3.86+) than that for the tetragonal modification (2.71+ - 3.08+).

The hydrogen reduction of Mn-Co oxides with the spinel structure was studied by *in situ* XRD, XPS, and TPR. It was found that the reduction of mixed oxides occurs in two stages. At the first

stage, the oxide  $(\text{Mn,Co})_3\text{O}_4$  transforms to  $(\text{Mn,Co})\text{O}$ . At the second stage, the solid solutions  $(\text{Mn,Co})\text{O}$  are reduced into metallic cobalt and  $\text{MnO}$ . The introduction of manganese into the structure of an oxide leads to an increase in the temperature of both stages, although to a different extent. Indeed, for the first stage, the structures of initial  $(\text{Mn,Co})_3\text{O}_4$  and intermediate  $(\text{Mn,Co})\text{O}$  oxides are similar, and conversion from one to another requires only a small displacement of cations. In contrast, the formation of metallic cobalt from  $(\text{Mn,Co})\text{O}$  requires rearrangement of the entire structure, which makes the effect of manganese cations on the second stage of reduction much more significant. The combined use of *in situ* XRD and *pseudo in situ* XPS made it possible to detect the initial stages of the process: the reduction begins in the volume of the solid solution, then cobalt segregates and forms nanoparticles on the oxide surface, and only after a long time, there appears the crystalline phase of metallic cobalt.

It was shown that the gradual change in the chemical composition of a mixed oxide is a very promising approach to obtain detailed information about the route of the reduction. In its turn, the combined usage of *in situ* techniques directly determines the chemical state of cations under reductive conditions.

AUTHOR INFORMATION

## Corresponding Author

**Olga A. Bulavchenko** – *Boreskov Institute of Catalysis, Novosibirsk 630090, Russia;*

*Novosibirsk State University, Novosibirsk 630090, Russia; orcid.org/0000-0001-5944-*

*2629; E-mail: [obulavchenko@catalysis.ru](mailto:obulavchenko@catalysis.ru)*

## Authors

**Tatyana N. Afonassenko** – *Center of New Chemical Technologies BIC, Omsk 644040, Russia*

**Anastasia V. Ivanchikova** – *Boreskov Institute of Catalysis, Novosibirsk 630090, Russia;*

*Novosibirsk State University, Novosibirsk 630090, Russia*

**Vadim Yu. Murzin** – *Deutsches Elektronen-Synchrotron, DESY, Hamburg D-22607, Germany*

**Anna M. Kremneva** – *Boreskov Institute of Catalysis, Novosibirsk 630090, Russia*

**Andrey A. Saraev** – *Boreskov Institute of Catalysis, Novosibirsk 630090, Russia; Novosibirsk*

*Vasily V. Kaichev* – *Boreskov Institute of Catalysis, Novosibirsk 630090, Russia; Novosibirsk*

**Sergey V. Tsybulya** – *Boreskov Institute of Catalysis, Novosibirsk 630090, Russia;*

*Novosibirsk State University, Novosibirsk 630090, Russia*

## Author Contributions

The manuscript was written through contributions of all authors. All authors have given approval to the final version of the manuscript.

## Notes

The authors declare no competing financial interest.

## ACKNOWLEDGMENT

The authors are grateful to the Ministry of Science and Higher Education of the Russian Federation (Project AAAA-A21-121011390011-4). O.A.B. acknowledges support from the Russian Foundation for Basis Research (Project No. 18-33-00542). The authors acknowledge PETRA III, DESY on P65 Beamline (in-house research, proposal # I-20180720), and Dr. V.A. Rogov for the TPR-H<sub>2</sub> measurements. The XPS experiments were performed using facilities of the shared research center “National center of investigation of catalysts” at Boreskov Institute of Catalysis.

## SUPPORTING INFORMATION



Supporting Information Available: XRD data (quantitative phase composition, lattice parameters, lattice volume, CSR and microstrains ( $\epsilon_0$ ) for the  $\text{Mn}_x\text{Co}_{3-x}$  oxides *in situ* XRD results for  $x=0.1$ , 1.1, 1.9, 2.3, 2.7. This material is available free of charge via the Internet at <http://pubs.acs.org>

## REFERENCES

1. Ruiz Puigdollers, A.; Schlexer, P.; Tosoni, S.; Pacchioni, G. Increasing Oxide Reducibility: The Role of Metal/Oxide Interfaces in the Formation of Oxygen Vacancies. *ACS Catalysis* **2017**, 7 (10), 6493-6513 DOI: 10.1021/acscatal.7b01913.
2. Lukashuk, L.; Yigit, N.; Rameshan, R.; Kolar, E.; Teschner, D.; Hävecker, M.; Knop-Gericke, A.; Schlögl, R.; Föttinger, K.; Rupprechter, G. Operando Insights into CO Oxidation on Cobalt Oxide Catalysts by NAP-XPS, FTIR, and XRD. *ACS Catalysis* **2018**, 8 (9), 8630-8641 DOI: 10.1021/acscatal.8b01237.
3. Dionigi, F.; Zeng, Z.; Sinev, I.; Merzdorf, T.; Deshpande, S.; Lopez, M. B.; Kunze, S.; Zegkinoglou, I.; Sarodnik, H.; Fan, D.; Bergmann, A.; Drnec, J.; Araujo, J. F.; Gliech, M.; Teschner, D.; Zhu, J.; Li, W. X.; Greeley, J.; Cuenya, B. R.; Strasser, P. In-situ structure and catalytic mechanism of NiFe and CoFe layered double hydroxides during oxygen evolution. *Nature Communications* **2020**, 11 (1), DOI: 10.1038/s41467-020-16237-1.
4. Kaichev, V. V.; Chesalov, Y. A.; Saraev, A. A.; Klyushin, A. Y.; Knop-Gericke, A.; Andrushkevich, T. V.; Bukhtiyarov, V. I. Redox mechanism for selective oxidation of ethanol

over monolayer V<sub>2</sub>O<sub>5</sub>/TiO<sub>2</sub> catalysts. *Journal of Catalysis* **2016**, 338, 82-93 DOI: 10.1016/j.jcat.2016.02.022.

5. Jalama, K.; Kabuba, J.; Xiong, H.; Jewell, L. L. Co/TiO<sub>2</sub> Fischer–Tropsch catalyst activation by synthesis gas. *Catalysis Communications* **2012**, 17, 154-159 DOI: <https://doi.org/10.1016/j.catcom.2011.10.029>.

6. Rochet, A.; Moizan, V.; Pichon, C.; Diehl, F.; Berliet, A.; Briois, V. In situ and operando structural characterisation of a Fischer–Tropsch supported cobalt catalyst. *Catalysis Today* **2011**, 171 (1), 186-191 DOI: <https://doi.org/10.1016/j.cattod.2011.03.079>.

7. Khassin, A. A.; Simentsova, I. I.; Shmakov, A. N.; Shtertser, N. V.; Bulavchenko, O. A.; Cherepanova, S. V. Effect of nitric oxide on the formation of cobalt-aluminum oxide structure from layered double hydroxide and its further transformation during reductive activation. *Applied Catalysis A: General* **2016**, 514, 114-125 DOI: 10.1016/j.apcata.2016.01.012.

8. Morales, F.; de Groot, F. M. F.; Glatzel, P.; Kleimenov, E.; Bluhm, H.; Hävecker, M.; Knop-Gericke, A.; Weckhuysen, B. M. In Situ X-ray Absorption of Co/Mn/TiO<sub>2</sub> Catalysts for Fischer–Tropsch Synthesis. *The Journal of Physical Chemistry B* **2004**, 108 (41), 16201-16207 DOI: 10.1021/jp0403846.

9. Popa, T.; Xu, G.; Barton, T. F.; Argyle, M. D. High temperature water gas shift catalysts with alumina. *Applied Catalysis A: General* **2010**, 379 (1), 15-23 DOI: <https://doi.org/10.1016/j.apcata.2010.02.021>.

10. Reddy, G. K.; Gunasekara, K.; Boolchand, P.; Smirniotis, P. G. Cr- and Ce-doped ferrite catalysts for the high temperature water-gas shift reaction: TPR and mossbauer spectroscopic study. *Journal of Physical Chemistry C* **2011**, 115 (4), 920-930 DOI: 10.1021/jp102959p.
11. Lee, D. W.; Lee, M. S.; Lee, J. Y.; Kim, S.; Eom, H. J.; Moon, D. J.; Lee, K. Y. The review of Cr-free Fe-based catalysts for high-temperature water-gas shift reactions. *Catalysis Today* **2013**, 210, 2-9 DOI: 10.1016/j.cattod.2012.12.012.
12. Kaichev, V. V.; Chesalov, Y. A.; Saraev, A. A.; Tsapina, A. M. A Mechanistic Study of Dehydrogenation of Propane over Vanadia-Titania Catalysts. *Journal of Physical Chemistry C* **2019**, 123 (32), 19668-19680 DOI: 10.1021/acs.jpcc.9b04991.
13. Toko, K.; Ito, K.; Saito, H.; Hosono, Y.; Murakami, K.; Misaki, S.; Higo, T.; Ogo, S.; Tsuneki, H.; Maeda, S.; Hashimoto, K.; Nakai, H.; Sekine, Y. Catalytic Dehydrogenation of Ethane over Doped Perovskite via the Mars-van Krevelen Mechanism. *Journal of Physical Chemistry C* **2020**, 124 (19), 10462-10469 DOI: 10.1021/acs.jpcc.0c00138.
14. Kabbour, H.; Gauthier, G. H.; Tessier, F.; Huvé, M.; Pussacq, T.; Roussel, P.; Hayward, M. A.; Moreno B, Z. L.; Marinova, M.; Colmont, M.; Colis, S.; Mentré, O. Topochemical Reduction of YMnO<sub>3</sub> into a Composite Structure. *Inorganic Chemistry* **2017**, 56 (14), 8547-8553 DOI: 10.1021/acs.inorgchem.7b01309.
15. Pussacq, T.; Mentré, O.; Tessier, F.; Löfberg, A.; Huvé, M.; Guerro Caballero, J.; Colis, S.; Kabbour, H. Nanometric nickel exsolution in the hexagonal perovskite Ba<sub>8</sub>Ta<sub>6</sub>NiO<sub>24</sub>: Survey of the structural, magnetic and catalytic features. *Journal of Alloys and Compounds* **2018**, 766, 987-993 DOI: <https://doi.org/10.1016/j.jallcom.2018.07.016>.

16. Trawiński, B.; Bochentyn, B.; Łapiński, M.; Kusz, B. A study of the kinetics of bismuth telluride synthesis by an oxide reduction method. *Thermochimica Acta* **2020**, 683, 178437 DOI: <https://doi.org/10.1016/j.tca.2019.178437>.
17. Svintsitskiy, D. A.; Kardash, T. Y.; Stonkus, O. A.; Slavinskaya, E. M.; Stadnichenko, A. I.; Koscheev, S. V.; Chupakhin, A. P.; Boronin, A. I. In situ XRD, XPS, TEM, and TPR study of highly active in co oxidation CuO nanopowders. *Journal of Physical Chemistry C* **2013**, 117 (28), 14588-14599 DOI: 10.1021/jp403339r.
18. Pike, J.; Hanson, J.; Zhang, L.; Chan, S.-W. Synthesis and Redox Behavior of Nanocrystalline Hausmannite (Mn<sub>3</sub>O<sub>4</sub>). *Chemistry of Materials* **2007**, 19 (23), 5609-5616 DOI: 10.1021/cm071704b.
19. Stobbe, E. R.; De Boer, B. A.; Geus, J. W. The reduction and oxidation behaviour of manganese oxides. *Catalysis Today* **1999**, 47 (1-4), 161-167.
20. Chen, H.; Zheng, Z.; Chen, Z.; Bi, X. T. Reduction of hematite (Fe<sub>2</sub>O<sub>3</sub>) to metallic iron (Fe) by CO in a micro fluidized bed reaction analyzer: A multistep kinetics study. *Powder Technology* **2017**, 316, 410-420 DOI: <https://doi.org/10.1016/j.powtec.2017.02.067>.
21. Bulavchenko, O. A.; Cherepanova, S. V.; Malakhov, V. V.; Dovlitova, L. S.; Ishchenko, A. V.; Tsybulya, S. V. In situ XRD study of nanocrystalline cobalt oxide reduction. *Kinetics and Catalysis* **2009**, 50 (2), 192-198 DOI: 10.1134/S0023158409020086.
22. Fedorov, A. V.; Kukushkin, R. G.; Yeletsky, P. M.; Bulavchenko, O. A.; Chesalov, Y. A.; Yakovlev, V. A. Temperature-programmed reduction of model CuO, NiO and mixed CuO–

NiO catalysts with hydrogen. *Journal of Alloys and Compounds* **2020**, 844, DOI: 10.1016/j.jallcom.2020.156135.

23. Wang, X.; Du, L. Y.; Du, M.; Ma, C.; Zeng, J.; Jia, C. J.; Si, R. Catalytically active ceria-supported cobalt-manganese oxide nanocatalysts for oxidation of carbon monoxide. *Physical Chemistry Chemical Physics* **2017**, 19 (22), 14533-14542 DOI: 10.1039/c7cp02004j.

24. Faure, B.; Alphonse, P. Co-Mn-oxide spinel catalysts for CO and propane oxidation at mild temperature. *Applied Catalysis B: Environmental* **2015**, 180, 715-725 DOI: 10.1016/j.apcatb.2015.07.019.

25. Zhang, Q.; Liu, X.; Fan, W.; Wang, Y. Manganese-promoted cobalt oxide as efficient and stable non-noble metal catalyst for preferential oxidation of CO in H<sub>2</sub> stream. *Applied Catalysis B: Environmental* **2011**, 102 (1-2), 207-214 DOI: 10.1016/j.apcatb.2010.11.043.

26. Tang, W.; Wu, X.; Li, S.; Li, W.; Chen, Y. Porous Mn-Co mixed oxide nanorod as a novel catalyst with enhanced catalytic activity for removal of VOCs. *Catalysis Communications* **2014**, 56, 134-138 DOI: <https://doi.org/10.1016/j.catcom.2014.07.023>.

27. Qu, Z.; Gao, K.; Fu, Q.; Qin, Y. Low-temperature catalytic oxidation of toluene over nanocrystal-like Mn-Co oxides prepared by two-step hydrothermal method. *Catalysis Communications* **2014**, 52, 31-35 DOI: <https://doi.org/10.1016/j.catcom.2014.03.035>.

28. Cheng, F.; Shen, J.; Peng, B.; Pan, Y.; Tao, Z.; Chen, J. Rapid room-temperature synthesis of nanocrystalline spinels as oxygen reduction and evolution electrocatalysts. *Nat. Chem.* **2011**, 3 (1), 79-84 DOI: 10.1038/nchem.931.

29. Sebastian, W.; R., J. G.; T., B. A. Synthesis and Characterization of Supported Cobalt–Manganese Nanoparticles as Model Catalysts for Fischer–Tropsch Synthesis. *ChemCatChem* **2014**, 6 (10), 2881-2888 DOI: doi:10.1002/cctc.201402260.
30. den Breejen, J. P.; Frey, A. M.; Yang, J.; Holmen, A.; van Schooneveld, M. M.; de Groot, F. M. F.; Stephan, O.; Bitter, J. H.; de Jong, K. P. A Highly Active and Selective Manganese Oxide Promoted Cobalt-on-Silica Fischer–Tropsch Catalyst. *Topics in Catalysis* **2011**, 54 (13), 768 DOI: 10.1007/s11244-011-9703-0.
31. Johnson, G. R.; Werner, S.; Bell, A. T. An Investigation into the Effects of Mn Promotion on the Activity and Selectivity of Co/SiO<sub>2</sub> for Fischer–Tropsch Synthesis: Evidence for Enhanced CO Adsorption and Dissociation. *ACS Catalysis* **2015**, 5 (10), 5888-5903 DOI: 10.1021/acscatal.5b01578.
32. Morales, F.; Grandjean, D.; de Groot, F. M. F.; Stephan, O.; Weckhuysen, B. M. Combined EXAFS and STEM-EELS study of the electronic state and location of Mn as promoter in Co-based Fischer-Tropsch catalysts. *Physical Chemistry Chemical Physics* **2005**, 7 (4), 568-572 DOI: 10.1039/B418286C.
33. Wu, M.; Zhan, W.; Guo, Y.; Guo, Y.; Wang, Y.; Wang, L.; Lu, G. An effective Mn-Co mixed oxide catalyst for the solvent-free selective oxidation of cyclohexane with molecular oxygen. *Applied Catalysis A: General* **2016**, 523, 97-106 DOI: 10.1016/j.apcata.2016.06.001.
34. Bulavchenko, O. A.; Gerasimov, E. Y.; Afonassenko, T. N. Reduction of double manganese-cobalt oxides: In situ XRD and TPR study. *Dalton Trans.* **2018**, 47 (47), 17153-17159 DOI: 10.1039/c8dt04137g.

35. Welter, E.; Chernikov, R.; Herrmann, M.; Nemausat, R. In *A beamline for bulk sample x-ray absorption spectroscopy at the high brilliance storage ring PETRA III*, AIP Conference Proceedings, 2019; 2019.
36. Ravel, B.; Newville, M. ATHENA, ARTEMIS, HEPHAESTUS: Data analysis for X-ray absorption spectroscopy using IFEFFIT. *Journal of Synchrotron Radiation* **2005**, 12 (4), 537-541 DOI: 10.1107/S0909049505012719.
37. Kaichev, V. V.; Chesalov, Y. A.; Saraev, A. A.; Tsapina, A. M. A Mechanistic Study of Dehydrogenation of Propane over Vanadia–Titania Catalysts. *The Journal of Physical Chemistry C* **2019**, 123 (32), 19668-19680 DOI: 10.1021/acs.jpcc.9b04991.
38. Scofield, J. H. Hartree-Slater subshell photoionization cross-sections at 1254 and 1487 eV. *J. Electron Spectrosc. Relat. Phenom.* **1976**, 8 (2), 129-137 DOI: 10.1016/0368-2048(76)80015-1.
39. Fairley, N. [www.casaxps.com](http://www.casaxps.com).
40. Shannon, R. D. Revised effective ionic radii and systematic studies of interatomic distances in halides and chalcogenides. *Acta Crystallographica Section A* **1976**, 32 (5), 751-767 DOI: 10.1107/S0567739476001551.
41. Manceau, A.; Gorshkov, A. I.; Drits, V. A. Structural chemistry of Mn, Fe, Co, and Ni in manganese hydrous oxides: Part I. Information from XANES spectroscopy. *American Mineralogist* **1992**, 77 (11-12), 1133-1143.

42. Kwon, O.-S.; Kim, M.-S.; Kim, K.-B. A study on the effect of lithium insertion–  
extraction on the local structure of lithium manganese oxides using X-ray absorption  
spectroscopy. *Journal of Power Sources* **1999**, 81-82, 510-516 DOI:  
[https://doi.org/10.1016/S0378-7753\(99\)00210-4](https://doi.org/10.1016/S0378-7753(99)00210-4).
43. Lima, F. H. B.; Calegaro, M. L.; Ticianelli, E. A. Investigations of the catalytic properties  
of manganese oxides for the oxygen reduction reaction in alkaline media. *Journal of*  
*Electroanalytical Chemistry* **2006**, 590 (2), 152-160 DOI:  
<https://doi.org/10.1016/j.jelechem.2006.02.029>.
44. Ressler, T.; Wong, J.; Roos, J.; Smith, I. L. Quantitative Speciation of Mn-Bearing  
Particulates Emitted from Autos Burning (Methylcyclopentadienyl)manganese Tricarbonyl-  
Added Gasolines Using XANES Spectroscopy. *Environmental Science & Technology* **2000**, 34  
(6), 950-958 DOI: 10.1021/es990787x.
45. Kunzl, V. A linear dependence of energy levels on the valency of elements. *Collect.*  
*Czech. Chem. Commun.* **1932**, 4, 213-224.
46. Kirby, J. A.; Goodin, D. B.; Wydrzynski, T.; Robertson, A. S.; Klein, M. P. State of  
manganese in the photosynthetic apparatus. 2. X-ray absorption edge studies on manganese in  
photosynthetic membrane. *JACS* **1981**, 103 (18), 5537-5542 DOI: 10.1021/ja00408a043.
47. Penner-Hahn, J. E.; Fronko, R. M.; Pecoraro, V. L.; Yocum, C. F.; Betts, S. D.; Bowlby,  
N. R. Structural characterization of the manganese sites in the photosynthetic oxygen-evolving  
complex using x-ray absorption spectroscopy. *JACS* **1990**, 112 (7), 2549-2557 DOI:  
10.1021/ja00163a011.



48. Penner-Hahn, J. E. In *Metal Clusters in Proteins*; American Chemical Society: 1988; Chapter 2, Vol. 372, pp 28-48.
49. Bencze, K. Z.; Kondapalli, K. C.; Stemmler, T. L. In *Encyclopedia of Inorganic Chemistry*; 2005.
50. Li, C.; Han, X.; Cheng, F.; Hu, Y.; Chen, C.; Chen, J. Phase and composition controllable synthesis of cobalt manganese spinel nanoparticles towards efficient oxygen electrocatalysis. *Nature Communications* **2015**, 6, 7345 DOI: 10.1038/ncomms8345  
<https://www.nature.com/articles/ncomms8345#supplementary-information>.
51. Jiao, F.; Frei, H. Nanostructured manganese oxide clusters supported on mesoporous silica as efficient oxygen-evolving catalysts. *Chemical Communications* **2010**, 46 (17), 2920-2922 DOI: 10.1039/b921820c.
52. Pankin, I. A.; Kravtsova, A. N.; Polozhentsev, O. E.; Budnyk, A. P.; Tsaturyan, A. A.; Bugaev, A. L.; Trigub, A. L.; Soldatov, A. V. X-ray spectroscopic diagnostics of the structure of quantum dots based on zinc and manganese sulfides and oxides. *Journal of Structural Chemistry* **2017**, 58 (8), 1633-1640 DOI: 10.1134/s0022476617080212.
53. Figueroa, S. J. A.; Requejo, F. G.; Lede, E. J.; Lamaita, L.; Peluso, M. A.; Sambeth, J. E. XANES study of electronic and structural nature of Mn-sites in manganese oxides with catalytic properties. *Catalysis Today* **2005**, 107-108, 849-855 DOI: <https://doi.org/10.1016/j.cattod.2005.07.156>.
54. Ramallo-López, J. M.; Lede, E. J.; Requejo, F. G.; Rodriguez, J. A.; Kim, J.-Y.; Rosas-Salas, R.; Domínguez, J. M. XANES Characterization of Extremely Nanosized Metal-Carbonyl

Subspecies (Me = Cr, Mn, Fe, and Co) Confined into the Mesopores of MCM-41 Materials. *The Journal of Physical Chemistry B* **2004**, 108 (52), 20005-20010 DOI: 10.1021/jp049241+.

55. Ressler, T.; Brock, S. L.; Wong, J.; Suib, S. L. Multiple-Scattering EXAFS Analysis of Tetraalkylammonium Manganese Oxide Colloids. *The Journal of Physical Chemistry B* **1999**, 103 (31), 6407-6420 DOI: 10.1021/jp9835972.

56. Bearden, J. A.; Burr, A. F. Reevaluation of X-Ray Atomic Energy Levels. *Reviews of Modern Physics* **1967**, 39 (1), 125-142 DOI: 10.1103/RevModPhys.39.125.

57. Jiang, T.; Ellis, D. E. X-ray absorption near edge structures in cobalt oxides. *Journal of Materials Research* **1996**, 11 (9), 2242-2256 DOI: 10.1557/JMR.1996.0285.

58. Liang, Y.; Wang, H.; Zhou, J.; Li, Y.; Wang, J.; Regier, T.; Dai, H. Covalent Hybrid of Spinel Manganese–Cobalt Oxide and Graphene as Advanced Oxygen Reduction Electrocatalysts. *Journal of the American Chemical Society* **2012**, 134 (7), 3517-3523 DOI: 10.1021/ja210924t.

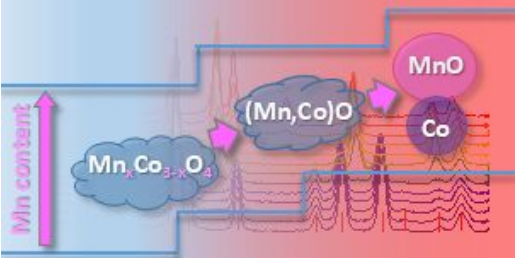
59. Bordeneuve, H.; Guillemet-Fritsch, S.; Rousset, A.; Schuurman, S.; Poulain, V. Structure and electrical properties of single-phase cobalt manganese oxide spinels  $\text{Mn}_{3-x}\text{Co}_x\text{O}_4$  sintered classically and by spark plasma sintering (SPS). *Journal of Solid State Chemistry* **2009**, 182 (2), 396-401 DOI: 10.1016/j.jssc.2008.11.004.

60. Arnoldy, P.; Moulijn, J. A. Temperature-programmed reduction of  $\text{CoO Al}_2\text{O}_3$  catalysts. *J. Catal.* **1985**, 93 (1), 38-54 DOI: 10.1016/0021-9517(85)90149-6.

61. Bulavchenko, O. A.; Cherepanova, S. V.; Tsybulya, S. V. In situ XRD investigation of  $\text{Co}_3\text{O}_4$  reduction. *Z. Kristallogr. Cryst. Mater.* **2009**, (30), 329-334 DOI: 10.1524/zksu.2009.0048.
62. Bukhtiyarova, M. V.; Ivanova, A. S.; Plyasova, L. M.; Litvak, G. S.; Rogov, V. A.; Kaichev, V. V.; Slavinskaya, E. M.; Kuznetsov, P. A.; Polukhina, I. A. Selective catalytic reduction of nitrogen oxide by ammonia on Mn(Fe)-substituted Sr(La) aluminates. *Applied Catalysis A: General* **2009**, 357 (2), 193-205 DOI: <https://doi.org/10.1016/j.apcata.2009.01.028>.
63. Biesinger, M. C.; Payne, B. P.; Grosvenor, A. P.; Lau, L. W. M.; Gerson, A. R.; Smart, R. S. C. Resolving surface chemical states in XPS analysis of first row transition metals, oxides and hydroxides: Cr, Mn, Fe, Co and Ni. *Applied Surface Science* **2011**, 257 (7), 2717-2730 DOI: 10.1016/j.apsusc.2010.10.051.
64. Oku, M.; Hirokawa, K.; Ikeda, S. X-ray photoelectron spectroscopy of manganese—oxygen systems. *J. Electron. Spectrosc. Relat. Phenom.* **1975**, 7 (5), 465-473 DOI: 10.1016/0368-2048(75)85010-9.
65. Castro, V. D.; Polzonetti, G. XPS study of MnO oxidation. *J. Electron Spectrosc. Relat. Phenom.* **1989**, 48 (1), 117-123.
66. Ramesh, K.; Chen, L.; Chen, F.; Liu, Y.; Wang, Z.; Han, Y.-F. Re-investigating the CO oxidation mechanism over unsupported MnO, Mn<sub>2</sub>O<sub>3</sub> and MnO<sub>2</sub> catalysts. *Catalysis Today* **2008**, 131 (1–4), 477-482 DOI: <http://dx.doi.org/10.1016/j.cattod.2007.10.061>.

67. Nesbitt, H. W.; Banerjee, D. Interpretation of XPS Mn(2p) spectra of Mn oxyhydroxides and constraints on the mechanism of MnO<sub>2</sub> precipitation. *American Mineralogist* **1998**, 83 (3-4), 305-315 DOI: 10.2138/am-1998-3-414.
68. Bulavchenko, O. A.; Afonassenko, T. N.; Sigaeva, S. S.; Ivanchikova, A. V.; Saraev, A. A.; Gerasimov, E. Y.; Kaichev, V. V.; Tsybulya, S. V. The Structure of Mixed Mn–Co Oxide Catalysts for CO Oxidation. *Topics in Catalysis* **2020**, 63 (1-2), 75-85 DOI: 10.1007/s11244-020-01230-1.
69. Khassin, A. A.; Yurieva, T. M.; Kaichev, V. V.; Bukhtiyarov, V. I.; Budneva, A. A.; Paukshtis, E. A.; Parmon, V. N. Metal–support interactions in cobalt-aluminum co-precipitated catalysts: XPS and CO adsorption studies. *Journal of Molecular Catalysis A: Chemical* **2001**, 175 (1-2), 189-204.
70. Kosova, N. V.; Devyatkina, E. T.; Kaichev, V. V. Optimization of Ni<sup>2+</sup>/Ni<sup>3+</sup> ratio in layered Li(Ni,Mn,Co)O<sub>2</sub> cathodes for better electrochemistry. *J. Power Sources* **2007**, 174 (2), 965-969 DOI: <https://doi.org/10.1016/j.jpowsour.2007.06.051>.
71. Venezia, A. M.; Murania, R.; Pantaleo, G.; Deganello, G. Nature of cobalt active species in hydrodesulfurization catalysts: Combined support and preparation method effects. *Journal of Molecular Catalysis A: Chemical* **2007**, 271 (1-2), 238-245 DOI: 10.1016/j.molcata.2007.02.039.

For Table of Contents Only



The introduction of manganese into the structure of  $\text{Mn}_x\text{Co}_{3-x}\text{O}_4$  inhibits the two stages of oxide reducibility